

Experimental study of permeability as a function of stress-induced damage in Stanstead granite

Steven Gaines^{1,2}, Mark Diederichs² and Ted Anderson¹

¹ Natural Resources Canada - CanmetMINING, Ottawa, Ontario, Canada

² Department of Geological Sciences and Geological Engineering – Queen's University, Kingston, Ontario, Canada



GeoCalgary
2022 October
2-5
Reflection on Resources

ABSTRACT

In most bedrock hydrogeological settings, planar discontinuities such as rock joints, bedding, or faults represent the dominant transport pathway, with permeability of the intact rock between these discontinuities generally considered negligible. However, assessment of intact rock permeability in otherwise intact bedrock surrounding excavations is an important consideration for evaluating long-term migration of contaminants surrounding underground infrastructure such as deep geological repositories, or for evaluation of potential migration pathways associated with gas storage or sequestration projects. Induced stresses surrounding underground excavations can result in localized rock damage that will experience an increase in permeability in proportion to the accumulation internal microcracks. Recent testing has been completed at CanmetMINING's Rock Mechanics Laboratory in Ottawa to better understand the relationship between crack damage thresholds preceding failure and intrinsic permeability. It was observed that as axial stress increased there was an initial decrease in the intrinsic permeability, followed by a slight increase following crack initiation (CI) until systematic crack interaction (CD) where a larger increase in permeability was measured.

RÉSUMÉ

Dans la plupart des contextes hydrogéologiques de la roche-mère, les discontinuités planes telles que les joints, le litage ou les failles représentent la voie de transport dominante, la perméabilité de la roche intacte entre ces discontinuités étant généralement considérée comme négligeable. Cependant, l'évaluation de la perméabilité de la roche intacte dans un substrat rocheux par ailleurs intact entourant les excavations est une considération importante pour évaluer la migration à long terme des contaminants autour des infrastructures souterraines telles que les dépôts géologiques profonds, ou pour évaluer les voies de migration potentielles associées aux projets de stockage ou de séquestration du gaz. Les contraintes induites autour des excavations souterraines peuvent entraîner des dommages localisés à la roche qui connaîtra une augmentation de la perméabilité proportionnelle à l'accumulation de micro-fissures internes. Des essais récents ont été réalisés au laboratoire de mécanique des roches de CanmetMINING à Ottawa afin de mieux comprendre la relation entre les seuils d'endommagement des fissures précédant la rupture et la perméabilité intrinsèque. On a observé que lorsque la contrainte axiale augmente, il y a une diminution initiale de la perméabilité intrinsèque, suivie d'une légère augmentation après l'initiation de la fissure (CI) jusqu'à l'interaction systématique des fissures (CD) où une augmentation plus importante de la perméabilité a été mesurée.

1 INTRODUCTION

The estimation of intact rock permeability and stress-induced permeability changes are important considerations for understanding long-term performance of underground containment facilities, such as deep geological repositories (DGRs) for nuclear waste, or for assessing migration pathways along damaged boreholes in underground gas storage operations.

Recently, a laboratory testing program was initiated at CanmetMINING's Rock Mechanics Laboratory in Ottawa, Ontario to investigate permeability changes in rock core resulting from stress induced damage. The following paper provides an overview of the lab testing methodology, describes the interpretation procedures and discusses preliminary results of this testing program.

2 BACKGROUND

It is well understood that stress redistribution around underground openings, as well as the method of excavation, can damage the surrounding rockmass and may contribute to changes to the near field permeability (e.g. Kelsall *et al.*, 1984; Martin *et al.*, 1997; Souley *et al.*, 2001; Siren *et al.*, 2015; Perras and Diederichs, 2016). For many applications, changes in permeability surrounding an excavation are inconsequential to overall ground stability or for estimates of dewatering requirements. However, detailed design of long-term repositories, or sequestration/storage projects that require isolation of fluids at depth, damage induced permeability may lead to preferential pathways for vertical or horizontal movement of the containment material (i.e. radionuclides, natural gas, carbon, hydrogen, etc.).

2.1 Stresses around a Circular Excavation

The simplest case of stress redistribution is illustrated in Figure 1, showing the relationship between the orientation of the principal stresses (in two-dimensions) and the zones of increased tangential stress and decreased stress.

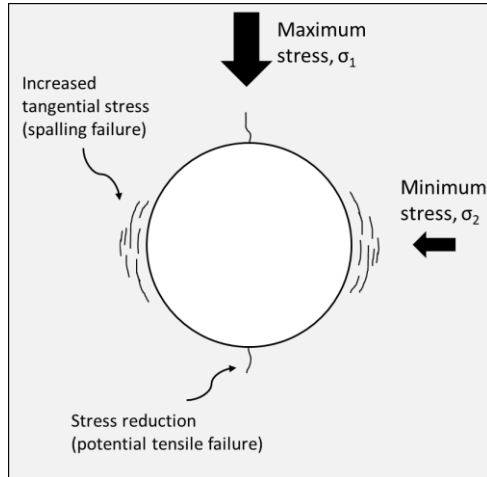


Figure 1. Distribution of tangential stresses around a circular opening relative to principal stress orientation.

As illustrated in Figure 1, the maximum induced compressive stresses around a circular opening are located normal to the maximum far field stress direction (σ_1), with a zone of reduced stress (stress shadow) located in the orientation of σ_1 . The maximum tangential stress can be estimated by the simplified form of the Kirsch solution, Equation 1.

$$\sigma_t = 3 \sigma_1 - \sigma_2 \quad [1]$$

Where: σ_t = tangential stress
 σ_1 = maximum far-field stress
 σ_2 = minimum far-field stress

In theory, the maximum disturbance related to stress redistribution will occur in the compressive zone and/or in the zone of reduced tangential stresses. For example, induced tangential stresses exceeding rock strength may develop new compression fractures. In cases where the stress ratio (σ_1/σ_2) is greater than three, negative hoop stresses develop in the zone of stress reduction, which can open pre-existing features, or initiate tensile fractures.

2.2 Excavation Damage Zone

The excavation damage zone (EDZ) refers to the zone surrounding an underground opening that has experienced disturbance resulting from a combination of stress induced fracturing and/or damage from the construction process. The processes and nomenclature associated with EDZs are well documented in the literature, notably by Perras and Diederichs (2016). A schematic, showing the relative distribution of damage zones surrounding an excavation, is provided as Figure 2.

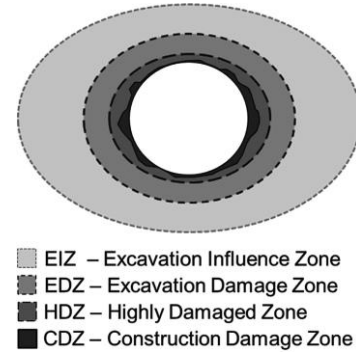


Figure 2. Illustration showing the distribution of damage zones surrounding a circular excavation (Perras and Diederichs, 2016).

2.3 Damage Thresholds

Although unconfined compressive strength (UCS) is a commonly used measurement of 'rock strength', it is important to recognize that damage is accumulated in otherwise intact rock prior to failure. It has been established that prior to peak strength there are damage thresholds in massive, brittle rock that can be defined by the behaviour of cylindrical specimens under compression (Bieniawski, 1967; Wawersik and Fairhurst, 1970; Eberhardt *et al.*, 1998; Diederichs, 2003; Diederichs *et al.*, 2004; Diederichs, 2007; Nicksiar and Martin, 2013). The stages of stress-strain behaviour in compression tests, noting the various crack damage thresholds, are shown in Figure 3.

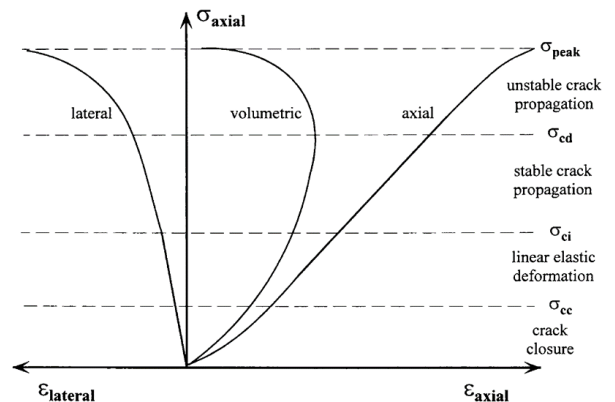


Figure 3. Stress-strain response in unconfined compression tests and identification of crack damage thresholds (Diederichs *et al.*, 2004 after Eberhardt *et al.*, 1998).

As illustrated in Figure 3, the onset of new specimen damage is identified as the crack initiation (CI) threshold. This is followed by a period of stable crack propagation until systematic crack interaction is reached, i.e. critical damage (CD). CD is considered the onset of sample yielding and represents the onset of unstable fracture propagation.

The stress conditions surrounding an open excavation are characterized by low confinement and high tangential

stresses normal to the maximum far field stress, and prone to development of slabbing parallel to the excavation wall. This is analogous to the generation of axial fractures parallel to loading in unconfined, or low confinement, compression tests. Diederichs (2003) developed an s-shaped failure envelope to better characterize the strength of brittle rocks to left of the spalling limit (Figure 4).

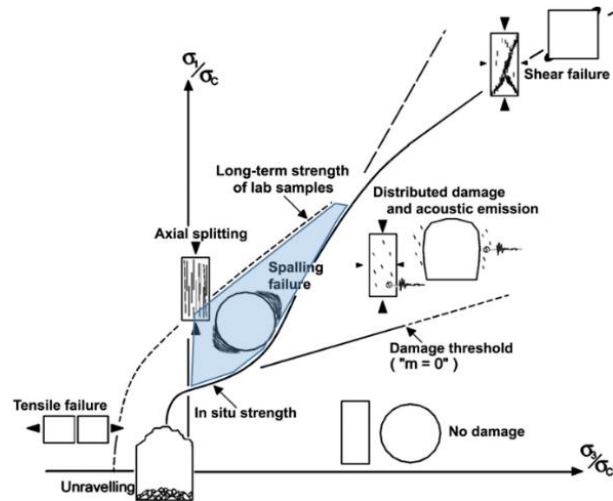


Figure 4. S-shaped failure envelope for brittle rock with the stress conditions considered in the study highlighted (modified from Diederichs, 2003).

3 TEST METHODOLOGY

3.1 Specimen Lithology

Stanstead grey granite (SGG) was used as the rock material for testing owing to its relatively homogeneous composition and availability of historical testing data. SGG is a light to medium grey, medium and coarse-grained granodiorite (MERN, 2022).

SGG specimens tested as part of this investigation had a nominal diameter of 75 mm. A photograph of representative SGG specimens is shown in Figure 5.



Figure 5. Specimens of Stanstead granite.

3.2 Compression Testing

Testing of SGG has been completed at CanmetMINING's Rock Mechanical Laboratory on SGG using the servo-controlled MTS 815 load frame. Additional specimens were

tested during this current study to confirm that material properties aligned with historical testing results, as well as to provide baseline data for comparing permeability testing results.

3.3 Permeability Testing

Intact rock permeability was estimated using the constant head (pressure) test, completed in general accordance with ASTM D2434: Standard Test Methods for Measurement of Hydraulic Conductivity of Coarse-Grained Soils (ASTM, 2022). Testing was completed on saturated specimens that had undergone vacuum saturation for a minimum of 72 hours.

Radially grooved platens were used with the MTS 815 frame to evenly distribute the water inflow (bottom) and outflow (top) ends of each specimen. To prevent flow from 'short-circuiting' the system (i.e. flowing along outside of the core) rubber tubing was positioned at the core-platen interfaces, and heat shrink sleeve was installed surrounding the core, rubber tubing and platens. Metal wire was used to tightly secure the rubber tube and sleeve above and below the interface (Figure 6).



Figure 6. Photographs showing a grooved platen used for permeability tests with the MTS load frame (left) and the platen installed at one end of the core sample (right).

An axial pre-load of 0.5 to 1 kN was applied to secure the platens. Confinement, S_3 , was applied radially to provide additional sealing of the sleeve against the platens and outer area of the core to ensure flow was directed through the sample.

Fluid inflow was controlled during the test using a built-in hydraulic module, which controls the inflow pressure. Pressure was measured at the input and discharge end using electronic pressure gauges with a servo-control feedback loop to the hydraulic system to control the flow volume, Q , such that a constant pressure, P_1 , was maintained. A schematic of the test setup used to conduct permeability tests is provided as Figure 7.

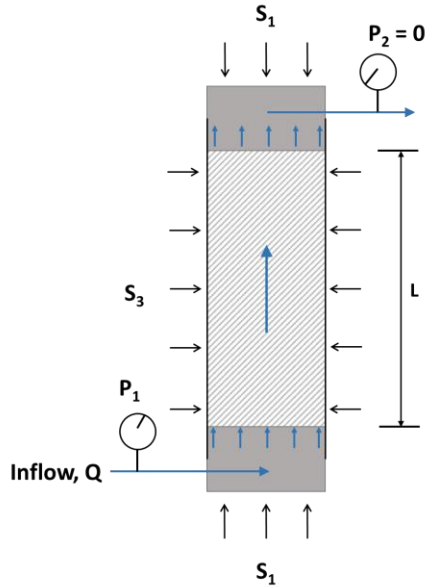


Figure 7. Schematic illustrating the test setup for core permeability tests.

The volume of water flowing into the specimen is measured precisely as a function of the piston displacement controlling inflow. This assumes an infinitely stiff system, which is reasonable given the relatively short length of stainless steel tubing connecting the reservoir with the bottom plate, and that the flow is directed through the sample.

Hydraulic tests on core specimens were conducted at three increasing pressure steps per test to estimate the permeability at each unique stress condition. The maximum inflow pressure, P_1 , did not exceed 60% of radial confinement, S_3 , to minimize the likelihood of leakage around the specimen. Once stable, each stage (pressure step) was run until a constant flow rate could be estimated, typically between 10 and 15 minutes.

Permeability was calculated using Darcy's law individually at each step, with the average permeability calculated as the mean of all of the pressure step tests. From Jaeger et al. (2007), Darcy's law can be presented in and rearranged to solve for permeability as Equation 2.

$$k = \frac{Q}{A} \cdot \frac{\mu \cdot L}{\Delta P} \quad [2]$$

Where: k = permeability [cm^2]
 Q = fluid flow [cm^3/s]
 A = cross-sectional area [cm^2]
 μ = fluid viscosity (0.001 Pa·s for water at 20°C)
 ΔP = pressure difference ($P_1 - P_2$) [Pa]
 L = sample length [cm]

The flow rate, Q , for each pressure step (P_1) was estimated using the slope of the best fit linear regression line on the volume versus time curve (cm^3/s) at steady state (i.e. negligible change in the flow rate). A typical permeability test is presented as Figure 8, showing the

relationships between pressure, time, fluid injection and flow rate.

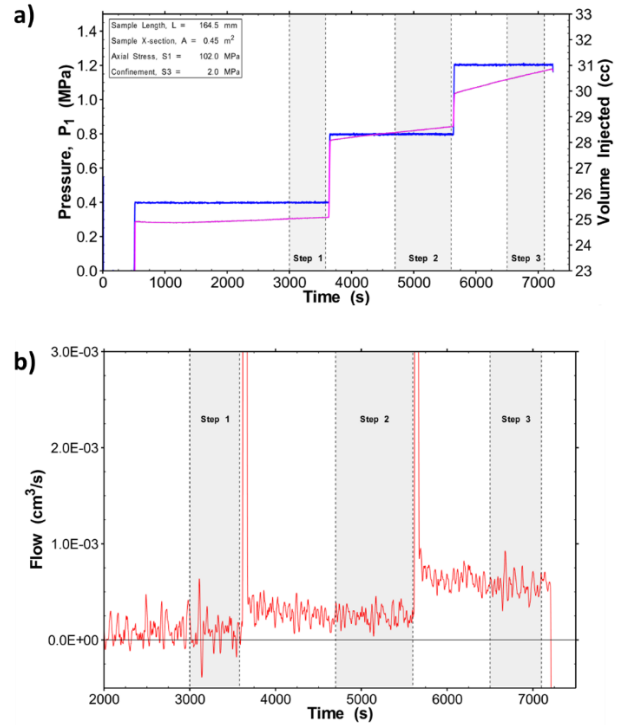


Figure 8. Typical permeability test results: a) showing the relationship between pressure, time and injection volume, and b) instantaneous flow rate.

Since outlet pressure, P_2 , is equal to zero, input pressure, $P_1 = \Delta P$. It can be seen in Figure 8a that pressure remains constant during each step, while the servo-control adjusts flow accordingly (Figure 8b). At each pressure step results were calculated over a window of observed constant pressure and flow determined by levelling off of the instantaneous flow rate (i.e. the change in flow as a function of time).

A total of five permeability tests were completed on a specimen of Stanstead granite to evaluate test methodology and gain insight on the relationship between laboratory stress-induced damage and permeability. The stress conditions for each test are summarized in Table 1.

Table 1. List of permeability tests and stress conditions.

Test Number	Confinement (MPa)	Axial Stress (MPa)
1	2.0 / 5.0 / 8.0	2.1 / 5.2 / 8.2
2	2.0	42.0
3	2.0	82.0
4	2.0	102.0
5	2.0	122.0

4 RESULTS

4.1 Physical and Mechanical Properties

Geomechanical testing of Stanstead granite has previously been conducted at CanmetMINING's Rock Mechanics Laboratory, and basic material properties are summarized in Table 2.

Table 2. Average properties of Stanstead grey granite

Rock Property	SGG ¹
UCS (MPa)	134.2
Young's Modulus (GPa)	47.7
Brazilian Tensile Strength (MPa)	7.0
Dry density (g/cm ³)	2.67
Porosity ² (%)	0.6

1) from Labrie (2017), average of 63 and 81mm diameter specimens
2) effective porosity estimated as part of current study

4.2 Damage Thresholds

Damage thresholds are rock type/material specific; however, it has been demonstrated that crack initiation typically ranges from 40 to 60% of peak strength (UCS), while the critical damage threshold (CD) is generally reached at 70-90% of peak strength (Hoek and Martin, 2014).

A comprehensive study of Stanstead granite based on testing completed at CanmetMINING was completed by Walton (2018), who interpreted Hoek-Brown strength parameters UCS, m_i , to characterize the peak, CI and CD strength envelopes. Figure 9 shows the strength envelopes of dry, 75 mm diameter specimens from Walton (2018).

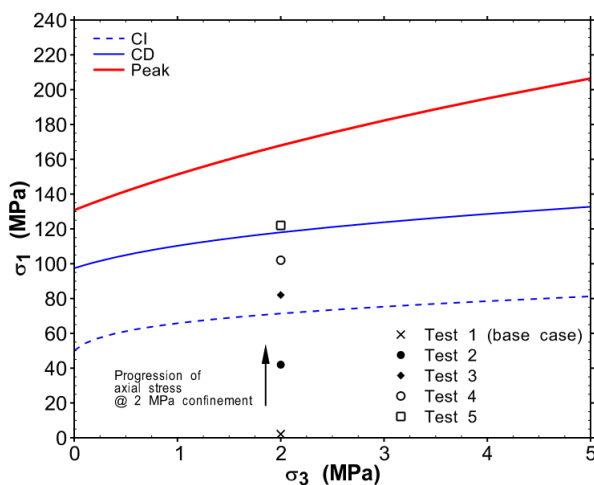


Figure 9. Generalized Hoek-Brown strength envelopes for Stanstead granite based on parameters summarized in Walton (2018) for 75 mm specimens.

As shown in Figure 9, at 2 MPa confinement, the CI, CD and peak thresholds were estimated at approximately 71, 118 and 168 MPa, respectively. To compare to historical results for SGG, three supplemental compression

tests were completed: one UCS (dry), one triaxial (2 MPa confinement, dry) and one triaxial (2 MPa confinement, saturated). The stress-strain curves for the three tests are shown on Figure 10.

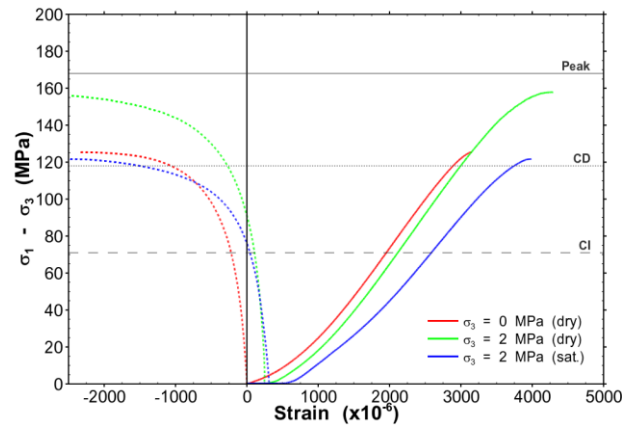


Figure 10. Stress-strain curves for SGG compression tests showing strength thresholds (dry) estimated at 2 MPa confinement from Walton (2018).

The supplemental SGG tests conducted on dry specimens (unconfined and at 2 MPa confinement) correlate well with the interpreted strength envelopes for 75 mm core provided in Walton (2018), as well as material properties summarized in Table 2. However, the saturated specimen experiences premature failure, failing at approximately 20 MPa less than the dry specimen at the same confinement. Although this test was completed under fully drained conditions, with the platens open to fluid flow out of the sample during compression, it is likely that the relatively low permeability resulted in an inability of pore fluid to escape the matrix leading to anomalous stress concentrations and failure. The poroelastic behaviour of specimens during compression tests is beyond the scope of this paper.

To more accurately compare permeability under various loading conditions the crack damage parameters, CI and CD, were estimated from the supplemental test conducted on the saturated specimen tested at 2 MPa confinement. CI was estimated using the inverse tangent lateral stiffness (ITLS) method, proposed by Ghazvinian *et al.* (2012). This method magnifies changes in the slope of the lateral strain versus axial stress to identify the stress level where the rate of lateral strain begins to increase. This increased rate of lateral strain is assumed to be due to dilation related to the systematic generation of microcracks, which under low confinement will be preferentially oriented in the direction of maximum loading.

Figure 11 presents the ITLS plot for the compression test completed on a saturated specimen at 2 MPa confinement, showing the interpreted CI threshold where the curve begins to deviate from linearity.

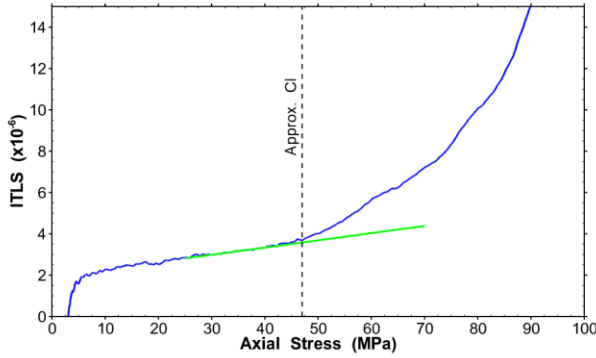


Figure 11. Inverse tangent lateral stiffness for the saturated specimen tested at 2 MPa of confinement.

As discussed in Section 2.3, the critical damage threshold represents the beginning of systematic crack interaction and onset of unstable crack growth characteristic of sample yield. Maximum volumetric strain (VSR) is one method for estimating the CD threshold in brittle rock (Martin and Chandler, 1994, which in unconfined compressive tests is coincident with the onset of axial stress-strain non-linearity and true yield (Deiderichs *et al.*, 2004). Although stiffness is not truly linear, the tangent modulus vs. stress curve presented in Figure 12 can also be used identify the start more rapid non-linear behaviour of the core specimen. In this case the approximate CD threshold is estimated where there is an increase in the rate of specimen softening, represented by a decrease in the slope of the tangent modulus curve.

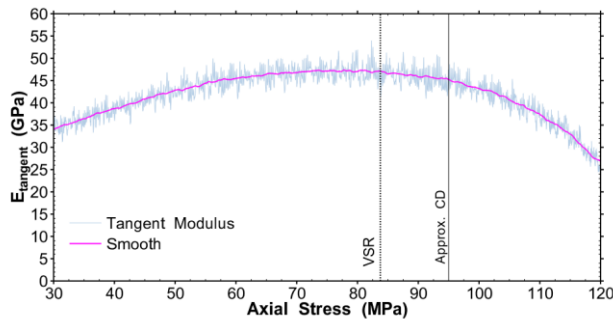


Figure 12. Tangent modulus showing stiffness as a function of axial stress at 2 MPa confinement.

In this case, VSR and the onset of axial stress-strain non-linearity are not coincident, but are both shown in Figure 12 to illustrate an approximate range of damage and crack interaction. Based on Figures 11 and 12, CI and CD thresholds of 47 and 95 MPa, respectively, are reasonable estimates for SGG (saturated) at 2 MPa confinement.

4.3 Core Permeability

Intrinsic permeability of SGG was estimated in a single specimen under variable stress conditions as described in Section 3.3. This included a series of tests conducted at increasing isostatic confinement, as well as series of tests at constant confinement while increasing the axial load (i.e. increasing differential stress). Results of permeability tests

completed under hydrostatic conditions are summarized in Table 3.

Table 3. Permeability results for SGG at 2, 5 and 8 MPa confinement (Test 1).

Confinement (MPa)	P ₁ (MPa)	Q (cm ³ /s)	k (cm ²)	k _{avg} (cm ²)
2	0.4	1.7E-04	1.6E-13	1.7E-13
	0.8	3.8E-04	1.7E-13	
	1.2	6.1E-04	1.8E-13	
5	0.4	--	--	7.3E-14
	0.8	1.1E-04	5.3E-14	
	1.2	3.0E-04	9.2E-14	
8	0.4	4.7E-05	4.5E-14	5.1E-14
	0.8	4.8E-05	2.3E-14	
	1.2	2.7E-04	8.4E-14	

-- = negligible flow, unable to estimate k.

The permeability estimates shown in Table 3 for each pressure step are fairly consistent, and the flow versus pressure relationship relatively linear, suggesting that the assumption of laminar flow is reasonable. There was higher scatter in the permeability estimates at 8 MPa confinement, which is due to the flow nearing the lower measureable threshold of the testing system. Overall, the results show that as confinement was increased there was a notable decrease in permeability (Figure 13). This decreased permeability is interpreted to be due to closure of existing microcracks, compression of existing pore space (which is minimal in SGG), and squeezing of grain boundaries. Results are consistent with other studies that have demonstrated a reduction in intrinsic permeability with increasing confinement due to closer microcracks and pore space (Zheng *et al.*, 2015; Glowacki and Selvadurai, 2016).

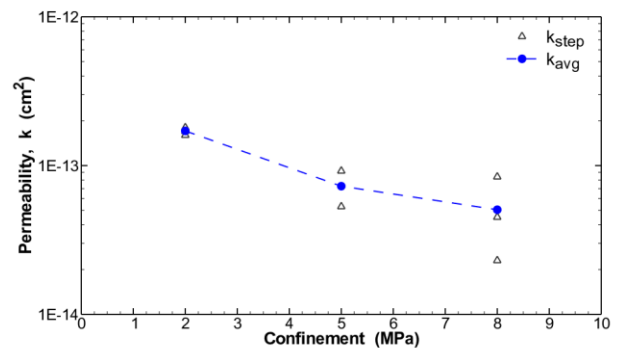


Figure 13. Relationship between intrinsic permeability and isostatic confinement in SGG.

Results for the differential loading tests are presented in Table 3 and illustrated in Figure 14. For this suite of tests radial stress (confinement) is held constant at 2 MPa and axial load/stress is increased to capture permeability at a set of unique stress conditions in order to correlate them to crack damage thresholds. These results show an initial decrease in permeability, followed by a relatively steady

increase in permeability beyond CI. Beyond CD there is a notable increase in the permeability

Table 3. Permeability results for SGG at 2 MPa confinement and increasing axial stress.

Test Number	Differential Stress, $\sigma_1 - \sigma_3$ (MPa)	Interpreted Damage	k_{avg} (cm ²)
1	0	none	1.7E-13
2	40	< CI	8.5E-14
3	80	> CI and < CD	1.1E-13
4	100	at CD	1.4E-13
5	120	> CD	3.3E-13

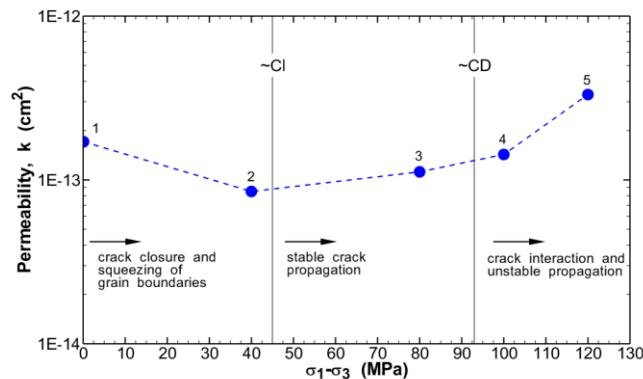


Figure 14. Permeability evolution with increasing axial stress at 2 MPa in SGG.

5 DISCUSSION

The effective porosity of Stanstead granite is less than 1%, therefore at low hydrostatic confinement flow through rock is interpreted to be dominated by movement along grain boundaries, with minimal flow occurring through existing microcracks or pore space. As isostatic confinement increases, flow is restricted by compression of the grain boundaries as well as closure of any existing microcracks and pore space. This general trend and observations are consistent with those reported in the literature (ex. Brace, 1968; Badrul Alam *et al.*, 2014; Glowacki and Selvadurai, 2016; Selvadurai and Glowacki, 2017).

As axial load increases horizontal grain boundaries and cracks are preferentially compressed. In addition, the Poisson's effect (i.e. lateral strain initiated from axial loading) will contribute to closure of vertically oriented radial microcracks, further decreasing apparent permeability. Test 2 represents this case, and observed permeability is similar to the estimate at 5 MPa of isostatic confinement.

Beyond CI new vertically oriented tensile microcracks are generated, which preferentially align with flow direction. This creates new pathways for fluid flow, however since microcracks are random and not well connected the result

in only a moderate increase in permeability. Lastly, at and beyond CD threshold the density of microcracks increases. Cracks begin to coalesce and interact and there is a more pronounced increase in the permeability owing to the interconnectivity of the fractures throughout the specimen.

6 CONCLUSIONS

Preliminary results from this study demonstrate that under low confinement, increasing axial stress preceding ultimate failure results in stress induced permeability changes that can be correlated to crack damage thresholds. The following observations can be made based on the results of this testing:

- Increased isostatic sample confinement decreases permeability. This is interpreted to be due to closure of existing microcracks, pore space and compression at grain boundaries.
- As axial stress increases under low confinement there is an initial decrease in permeability prior to the CI threshold. The decrease in permeability is similar to the effect of increasing isostatic confinement and related to crack closure and compression of grain boundaries. Horizontal features will be closed/compressed more rapidly, followed by vertical features that will experience closure due to the Poisson's effect, with grains undergoing lateral strain due to axial loading.
- Following CI, an increase in permeability is observed related to the generation of new damage within the specimen. In this region, microcracks are poorly interconnected, therefore only a moderate increase in permeability is observed even as the density of microcracks increases.
- At crack interaction (CD) and beyond there is sufficient damage and connectivity that fluid moves preferentially through interconnected microcracks. This results in a more prominent increase in permeability.

7 LIMITATIONS AND FUTURE WORK

These initial results suggest that there is a measurable change in laboratory scale permeability in relatively low porosity and permeability rock that is related to material crack damage thresholds. Additional testing is needed at more axial stress levels to improve the resolution and strengthen the relationship between permeability and damage thresholds. Furthermore, additional tests using Stanstead granite and other similar crystalline rocks, as well as brittle sedimentary rocks, are required to confirm these findings.

The completion of steady state, constant head permeability tests using water as a fluid medium is time consuming, hence only limited testing has been conducted to-date. It is recognized that flow values are approaching the lower measurable limit of the current testing equipment, therefore lengthening test duration, or using a less viscous fluid such as nitrogen may provide better flow resolution.

8 ACKNOWLEDGMENTS

This work was funded by CanmetMINING as part of an internal research program associated with improving laboratory characterization of coupled hydro-mechanical behaviour of rock. The assistance from laboratory staff with the preparation of rock specimens, particularly Clinton DeRushie, is appreciated. Discussion and valuable input from Robert Walsh, Gabe Walton and Denis Labrie during this testing program and preparation of the paper is also acknowledged.

REFERENCES

- ASTM, 2022. D2434-22: Standard Test Methods for Measurement of Hydraulic Conductivity of Coarse-Grained Soils. ASTM International, PA, USA.
- Badrul Alam, A.K.M, Niioka, M., Fujii, Y., Fukuda, D., Kodama, J. 2014. Effects of confining pressure on the permeability of three rock types under compression. *Int. J. Rock Mech. Min. Sci.* 65: 49-61.
- Bieniawski, Z.T. 1967. Mechanism of Brittle Fracture of Rock: Part I – Theory of the Fracture Process. *Int. J. Rock Mech. Min. Sci.* 4: 395-406.
- Brace, W.F., Walsh, J.B., Frangos, W.T. 1968. Permeability of Granite under High Pressure. *Journal of Geophysical Research.* 73(6).
- Diederichs, M.S. 2003. Rock Fracture and Collapse Under Low Confinement Conditions. *Rock Mechanics and Rock Engineering.* 36(5): 339-381.
- Diederichs, M.S., Kaiser, P.K. and Eberhardt, E. 2004. Damage initiation and propagation in hard rock during tunneling and the influence of near-face stress rotation. *Int. J. Rock Mech. Min. Sci.* 41: 785-812.
- Diederichs, M.S. 2007. The 2003 Canadian Geotechnical Colloquium: Mechanistic interpretation and practical application of damage and spalling prediction criteria for deep tunnelling. *Canadian Geotechnical Journal.* 44(9).
- Eberhardt, E., Stead, D., Stimpson, B. and Read, R.S. 1998. Identifying crack initiation and propagation thresholds in brittle rock. *Canadian Geotechnical Journal.* 35: 222-233.
- Glowacki, A. and Selvadurai, A.P.S. 2016. Stress-induced permeability changes in Indiana Limestone. *Engineering Geology.* 215: 122-130.
- Hoek, E. and Martin, C.D. 2014. Fracture initiation and propagation in intact rock – A review. *Journal of Rock Mechanics and Geotechnical Engineering.* 6: 287-300.
- Jaeger, J.C., Cook N.G.W. and Zimmerman, R. 2007. Fundamentals of Rock Mechanics, 4th ed., Blackwell Publishing, MA, USA.
- Kelsall, P.C., Case, J.B. and Chabannes, C.R. 1984. Evaluation of Excavation-induced Changes in Rock Permeability. *Int. J. Rock Mech. Min. Sci. and Geomech. Abstr.* 21(3): 123-135.
- Labrie, D. 2017. Frictional properties of rocks as a function of rock type, specimen size and confining pressure. *Proceedings: 51st US Rock Mechanics/Geomechanics Symposium (ARMA)*, San Francisco, USA. June.
- Martin, C.D., Read, R.S. and Martino, J.B. 1997. Observations of Brittle Failure Around a Circular Test Tunnel. *Int. J. Rock Mech. Min. Sci.* 34(7): 1065-1073.
- MERN, 2022. Energie et Ressources naturelles Quebec. <https://mern.gouv.qc.ca/english/mines/industry/architectural/architectural-quarrying-stones-granite-grey-stanstead-grey-de.jsp>
- Nicksair, M. and Martin, C.D. 2013. Crack initiation stress in low porosity crystalline and sedimentary rocks. *Engineering Geology.* 154: 64-76.
- Perras, M.A. and Diederichs, M.S. 2016. Predicting excavation damage zone depths in brittle rocks. *Journal of Rock Mechanics and Geotechnical Engineering.* 8: 60-74.
- Selvadurai, A.P.S. and Glowacki, A. 2017. Stress-Induced Permeability Alterations in an Argillaceous Limestone. *Rock Mechanics and Rock Engineering.* 50: 1079-1096.
- Siren, T., Kantia, P. and Rinne, M. 2015. Considerations and observations of stress-induced and construction-induced excavation damage zone in crystalline rock. *Int. J. Rock Mech. Min. Sci.* 73: 165-174.
- Souley, M., Homand, F., Pepa, S. and Hoxha, D. 2001. Damage-induced permeability changes in granite: a case example at the URL in Canada. *Int. J. Rock Mech. Min. Sci.* 38: 297-310.
- Walton, G. 2018. Scale Effects Observed in Compression Testing of Stanstead Granite Including Post-peak Strength and Dilatancy. *Geotechnical and Geological Engineering.* 36: 1091-1111.
- Wawersik, W.R. and C. Fairhurst, 1970. A Study of Brittle Rock Fracture in Laboratory Compression Experiments. *Int. J. Rock Mech. Min. Sci.* 7: 561-575.
- Zheng, J., Zheng, L. Liu, H-H and Ju, Y. 2015. Relationships between permeability, porosity and effective stress for low-permeability sedimentary rock. *Int. J. Rock Mech. Min. Sci.* 78: 304-318.